



# The Contribution of M-dwarf Flares to the Thermal Escape of Potentially Habitable Planet Atmospheres

Laura N. R. do Amaral<sup>1</sup> , Rory Barnes<sup>2</sup> , Antígona Segura<sup>1</sup> , and Rodrigo Luger<sup>3,4</sup>

<sup>1</sup> Instituto de Ciencias Nucleares, Universidad Nacional Autónoma de México, Cto. Exterior S/N, C.U., Coyoacán, 04510 Ciudad de Mexico, CDMX; [laura.nevesdoamaral@gmail.com](mailto:laura.nevesdoamaral@gmail.com)

<sup>2</sup> Department of Astronomy, University of Washington, Seattle, WA 98105, USA

<sup>3</sup> Center for Computational Astrophysics, Flatiron Institute, 162 Fifth Ave, New York, NY 10010, USA

<sup>4</sup> NASA Virtual Planetary Laboratory Lead Team, USA

Received 2021 August 10; revised 2022 January 24; accepted 2022 February 2; published 2022 March 23

## Abstract

The habitability of planets around M dwarfs ( $\lesssim 0.5 M_{\odot}$ ) can be affected by the X-rays + extreme UV (XUV) emission of these stars, with flares occasionally increasing the XUV flux by more than 2 orders of magnitude above quiescent levels. This wavelength range can warm and ionize terrestrial planets' upper atmospheres, which expands the planetary radius and promotes atmospheric loss. In this work, we study the contribution of the XUV flux due to flares on the atmospheric escape of Earth-like planets orbiting M dwarfs through numerical simulations. We considered the first Gyr of planets with initial surface water abundances between 1 and 10 terrestrial oceans (TO), a small primordial hydrogen envelope ( $\leq 10^{-3} M_{\oplus}$ ), and with host-star masses between 0.2 and  $0.6 M_{\odot}$ . In this parameter range, we find that flares can remove up to two TO more than nonflaring stars, which, in some cases, translates to a doubling of the total water loss. We also find that flaring can increase atmospheric oxygen partial pressures by hundreds of bars in some cases. These results were obtained by adding a new module for flares to the VPPlanet software package and upgrading its atmospheric escape module to account for Roche lobe overflow and radiation/recombination-limited escape.

*Unified Astronomy Thesaurus concepts:* Stellar flares (1603); Exoplanet atmospheres (487); Star-planet interactions (2177); Habitable planets (695)

## 1. Introduction

Given the habitability of the Earth, it is reasonable to assume that potentially habitable planets may similarly consist of an iron-silicate interior and a liquid water surface ocean. For the purposes of this work, we will call such planets "Earth-like" planets.

To maintain surface water, the planet must have an atmosphere with greenhouse gases, which provides the pressure and temperature profile to maintain liquid water and avoid catastrophic water escape (Watson et al. 1981; Kasting 1988; Barnes et al. 2013; Wordsworth & Pierrehumbert 2013; Luger & Barnes 2015).

As water is a solvent for a large number of biochemical reactions that facilitate prebiotic chemistry (Cockell et al. 2016), any process that can remove it is relevant for the search for life in the universe. Here we consider how X-rays + extreme UV (XUV; 0.1–100 nm; Ribas et al. 2005) emission from stellar flares can photolyze atmospheric water and drive hydrogen escape to assess stellar flares impact on planetary habitability.

In order for a planet's surface temperature to be in the range for liquid water, the planet must receive an appropriate amount of energy from its star. The range of orbits around a particular star for which this condition is met for Earth-like planets is often called the habitable zone (HZ; Dole 1964; Kasting et al. 1993; Kopparapu 2013). The M stars ( $0.07$ – $0.6 M_{\odot}$ ) of the main sequence (also called M dwarfs) are currently the most

observationally accessible targets for the search and characterization of Earth-like exoplanets (Billings 2011; Shields et al. 2016; Fujii et al. 2018) because most stars are M dwarfs (Bochanski et al. 2010), and Earth-like planets are relatively large and massive compared to their host star. Moreover, these stars stay on the main sequence (MS) stage for  $10^{11}$  yr (Laughlin et al. 1997; Baraffe et al. 1998; Dotter et al. 2008), which is clearly much longer than the time it took for life to emerge on Earth. Preliminary reconnaissance of M dwarfs has revealed that 50% host an Earth-like planet (Garrett et al. 2018; Tuomi et al. 2019), so the Galaxy may be teeming with Earth-sized planets orbiting in the HZ of these low-mass stars.

However, the habitability of M-dwarf planets can be severely compromised by certain characteristics of these stars. For example, M dwarfs may require billions of years to reach the main sequence (Hayashi 1966; Laughlin et al. 1997; Baraffe et al. 1998), during which time these stars can follow the Hayashi track for over 1 billion years, with luminosities that can be over 1000 times larger than their zero-age main sequence luminosities. This change causes the HZ to move inward until the stars' cores begin to burn hydrogen (Ramirez & Kaltenegger 2014; Luger & Barnes 2015; Tian & Ida 2015). Once on the MS, the typical HZ for an M dwarf is at  $\leq 0.25$  au (Kasting et al. 1993). Luger & Barnes (2015) studied the impact of the pre-MS evolution (PMS) of the XUV radiation on M-dwarf planets and found that planets in the MS HZ might have experienced millions to billions of years of desiccating conditions, potentially rendering them dry and uninhabitable today. Additionally they showed that the desiccation process (water photolysis followed by hydrogen escape) could produce thousands of bars of oxygen. On the other hand, Luger et al. (2015) demonstrated that water escape can be suppressed if 1%



Original content from this work may be used under the terms of the [Creative Commons Attribution 4.0 licence](#). Any further distribution of this work must maintain attribution to the author(s) and the title of the work, journal citation and DOI.

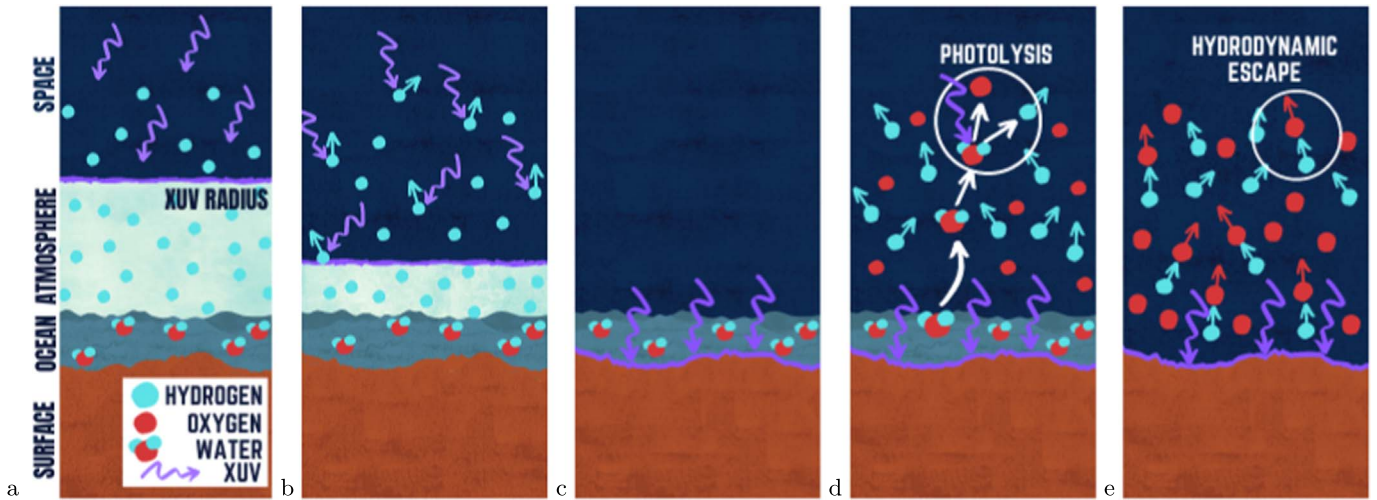


**Figure 1.** Schematic of atmospheric and surface water escape in our model. The darkest blue represents space, and the lighter blue backgrounds, from top to bottom, represent the H envelope, the troposphere, and the ocean. The brown background (at the bottom of the figure) represents the planetary surface. The light blue dots are the hydrogen atoms, and the red dots the oxygen atoms. The purple arrows are the XUV radiation incoming from the planet. The horizontal purple curve is the XUV radius (where the optical depth of XUV is unity). See description in the text for more details. [Plots/Scheme](#).

of the planet’s initial mass is in the form of a hydrogen atmosphere. In such a “habitable evaporated core” scenario, the hydrogen envelope insulates the water from the XUV radiation. Barnes et al. (2016) applied this model to Proxima Centauri b and found that it could lose 5 times the water content of the modern Earth during the pre-main sequence.

Another feature of M dwarfs is their strong variations in X-ray and extreme ultraviolet wavelengths, e.g., through stellar flares. Compared to the Sun, M-dwarf flares are more frequent and energetic (relative to the bolometric luminosity). While for the Sun the most energetic flares reach  $10^{32}$  ergs and occur about once per solar cycle (Youngblood et al. 2017), for some M dwarfs, flare events with this same energy (or more) happen every day (Audard et al. 2000; Hawley et al. 2014). Tilley et al. (2019) showed that UV radiation and proton fluxes from repeated flaring can deplete the ozone layer of an Earth-like planet by 94% over 10 yr, so the oxygen left over from photolysis may be elemental. Estrela et al. (2020) analyzed the impact of the UV radiation from flares on the potentially habitable planets of TRAPPIST-1 (an M8V star) and found that organisms that are nonresistant to UV could survive only if their habitats are deeper than 8 m below an ocean surface, or if the planet has an ozone layer. These studies highlight the importance of considering flares when assessing a planet’s habitability.

The XUV radiation emitted by M dwarfs (by chromospheric sources and flare events) ionizes and heats the exosphere of planetary atmospheres, slightly displacing it from hydrostatic equilibrium (Murray-Clay et al. 2009). This process generates an expansion of the atmosphere, where the exobase increases its radius, facilitating the escape because the cross section of the atmosphere increases during periods of high levels of XUV radiation (i.e., when the flaring is more frequent or when the star is more active) than in quiet periods (France et al. 2020). Previous works have analyzed some of the impacts of XUV radiation from flares in the atmospheric escape of planets. A study by Atri & Mogan (2021) showed that XUV from flares (with a constant rate through the time) can drive, over 1 Gyr, escape rates of  $3.38 \times 10^{-4} M_{\oplus}$ ,  $3.35 \times 10^{-4} M_{\oplus}$ ,  $1.46 \times 10^{-4} M_{\oplus}$  for planets around stars of M4–M10, M0–M4, and FGK

types, respectively. Similarly, a study by France et al. (2020) analyzed the impact of three flares from Barnard’s star in the atmosphere of an (unmagnetized) Earth-like planet and showed that these events can drive off the equivalent of  $\sim 90$  Earth atmospheres in a period of 1 Gyr.

Despite the impressive research into flaring and atmospheric escape, no study has yet evaluated how XUV emission from flares affects water loss and oxygen buildup in the atmospheres of planets orbiting M dwarfs. In this work, we present such analysis. To complete this task, we created a new module in the numerical code VPLanet (Barnes et al. 2020) that simulates the contribution of XUV by flares to the incident flux on an Earth-like planet and the resultant water photolysis, hydrogen escape, and oxygen accumulation. We employ a model for flares for stars between 0.2 and  $0.6 M_{\odot}$  (Davenport et al. 2019) and have added this module, called FLARE, to the VPLanet codebase.<sup>5</sup>

We divide this paper into the following sections. In Section 2, we describe and validate the FLARE module. In Section 2.5 we explain the simulated physical systems. Section 3 shows the results of the flare’s influence when the model was applied to planets with a mass between 0.5 and  $5 M_{\oplus}$  around different M dwarf types and to four real planets. In Section 4, we discuss the results, and in Section 5 we present the conclusions of our work. Note that the source code, simulation data, the input files, and the scripts that generate the figures and the figures are available online.<sup>6</sup>

## 2. Model Description

In this section we present our physical models and numerical methods for simulating flares and atmospheric escape. To perform our simulations, we use the VPLanet software package that couples these processes. For this investigation, we have developed a new module for stellar flaring called FLARE, so we also present the validation of this model in this section.

<sup>5</sup> VPLanet is publicly available at <https://github.com/VirtualPlanetaryLaboratory/VPLanet>.

<sup>6</sup> <https://github.com/lauraamaral/WaterEscapeFlares> and <https://github.com/VirtualPlanetaryLaboratory/VPLanet>

Figure 1 illustrates the physical processes in our model, which assumes all relevant planets form with an H envelope. The first panel, 1(a), shows the system at the beginning of the simulation. Here, the XUV radiation (purple wiggly arrows) is interacting with the upper atmosphere of the planet (light blue). The model assumes the XUV radius  $R_{\text{XUV}}$ , i.e., where the optical depth of the atmosphere to XUV photons is unity, is the same as the planet radius, including the atmosphere (see Salz et al. 2016 for discussion on the validity of this assumption). This choice means that XUV radiation does not penetrate deep into the atmosphere but follows the planetary radius boundary. This XUV energy interacting with the particles in the atmosphere increases its temperature and promotes its expansion, pushing out the exobase and increasing escape. Thus, as the radius of the planet decreases, the XUV radius approaches the planetary surface (brown), as seen in Figure 1(b).

After the primordial atmosphere has escaped (Figure 1(c)), water in the stratosphere can absorb XUV photons and break apart into oxygen and hydrogen (see Figure 1(d)). This process can only occur if water can penetrate the tropopause, which we assume always occurs for planets orbiting interior to the HZ. If the hydrogen escape is vigorous enough, then oxygen can be dragged along with the hydrogen (Hunten et al. 1987), as shown in Figure 1(e).

### 2.1. VPLanet

To model the system, we use the software package VPLanet (Barnes et al. 2020), which combines semi-analytical models to estimate the time evolution of parameters associated with planetary evolution and habitability. The code simulates how planetary system properties like stellar characteristics and orbital parameters affect the liquid water on the planetary surface. It currently has 12 modules that calculate the contribution of the different planetary system properties. In the present work, we use three modules: STELLAR and AtmEsc, which simulate stellar evolution and atmospheric escape, respectively, as well as a new module, named FLARE, to simulate stellar flaring. We next discuss each of these modules.

### 2.2. Atmospheric Escape: AtmEsc

To simulate atmospheric loss due to high-energy radiation, we use VPLanet’s AtmEsc module that accounts for the loss of a primordial hydrogen envelope, as well as water photolysis followed by hydrogen and oxygen escape.

#### 2.2.1. Envelope Loss

The initial version of AtmEsc in VPLanet (Barnes et al. 2020) could only treat atmospheric escape as an energy-limited process, i.e., the flux of high-energy photons is the bottleneck for escape, not the supply of molecules and elements that are available to escape (diffusion-limited). Energy-limited escape generally takes the following form:

$$\dot{M}_{\text{EL}} = \frac{\epsilon_H F_{\text{XUV}} R_{\text{XUV}}}{4GM_{\text{XUV}} K_{\text{tide}} m_{\text{H}}}, \quad (1)$$

where  $\dot{M}_{\text{EL}}$  is the energy-limited mass-loss rate,  $F_{\text{XUV}}$  is the XUV energy flux,  $M_p$  is the mass of the planet,  $R_{\text{XUV}}$  is the radius where XUV is absorbed and mass is escaping to space (we assume it equals the planet radius  $R_p$ ), and  $\epsilon_{\text{XUV}} \approx 0.1$  is the XUV absorption efficiency (Watson et al. 1981). Erkaev

et al. (2007) introduced  $K_{\text{tide}}$  to approximate the decrease in escape velocity at the top of the planet’s envelope due to the host star’s gravity. They showed by scaling distances to the ratio of the Roche lobe radius  $R_{\text{Roche}}$  to the XUV radius  $R_{\text{XUV}}$ :

$$\chi = \frac{R_{\text{Roche}}}{R_{\text{XUV}}}, \quad (2)$$

where

$$R_{\text{Roche}} = \left( \frac{M_p}{3M_*} \right)^{1/3} a; \quad (3)$$

one could expand the gravitational potential to derive a relatively simple expression for the suppression of the local planetary gravity due to the nearby star. When  $m_p \ll M_*$ , as for the case of mini-Neptunes and main-sequence stars, Erkaev et al. (2007) showed that

$$K_{\text{tide}} \approx 1 - \frac{3}{2\chi} + \frac{1}{2\chi^3}. \quad (4)$$

For Earth-sized planets in the HZs of M dwarf stars,  $K_{\text{tide}}$  is typically between 0.9 and 0.99, so the effect is modest (see also Luger et al. 2015), but its inclusion does increase the accuracy of the model.

For the radius of the planet, we interpolate the grids from the work of Lopez et al. (2012), which are self-consistent models of “mini-Neptunes” over a range of masses and instellations. These grids take into account the evolution of the radius of the planet as the envelope contracts and entropy grows, independent of atmospheric escape. As mass is lost, AtmEsc also interpolates between planetary masses. In all cases, we assume the water content does not affect planetary radius as the global ocean mass is always less than 0.2% the planetary mass for all cases we simulate.

Another study by Turbet et al. (2020) showed that water-rich atmospheres can be an important factor to take into account in the mass–radius relation of water-rich rocky planets. In addition to the presence of water considered by Turbet et al. (2020), Lopez et al. (2012) also consider hydrogen and helium atmospheres. Thus, we decide to use the mass–radius relation from Lopez et al. (2012).

We have now updated this module to include radiation/recombination-limited (RR) escape (Murray-Clay et al. 2009) and Roche lobe overflow, which we will call “Bondi-limited” escape (Owen & Wu 2016). The former occurs when the planetary radius is smaller than the Roche limit and the incident XUV flux in the planet is energetic enough to drive hydrogen ionization, which lowers the escape rate because some energy that could drive escape goes into ionization.

In SI units, RR-limited escape rate can be expressed as

$$\dot{M}_{\text{RR}} = 2.248 \times 10^6 \left( \frac{F_{\text{EUV}}}{\text{W m}^{-2}} \right)^{1/2} \left( \frac{R_p}{R_{\oplus}} \right)^{3/2} \text{kg s}^{-1}, \quad (5)$$

where  $\dot{M}_{\text{RR}}$  is the mass-loss rate, and  $F_{\text{EUV}}$  is the extreme-UV energy flux incident on the planet. EUV observations are scarce (e.g., France et al. 2019) and to constrain the flux in this wavelength range, we must rely either on reconstructions using X-rays or FUV measurements (Sanz-Forcada et al. 2011; Linsky et al. 2013), stellar models (Fontenla et al. 2016; Peacock et al. 2020), or use semiempirical methods (Duvvuri

et al. 2021). Given the uncertainties associated to the calculation of the EUV flux and the large differences among the fluxes obtained by the different approximations (see, for example, Figure B1 in Peacock et al. 2020, or Section 7 in Duvvuri et al. 2021), we used the same flux for EUV and XUV. This means that our EUV flux is overestimated, which is consistent with our purpose of studying the worse case scenario for atmospheric loss.

The RR limit occurs when the incident XUV reaches a critical value:

$$F_{\text{crit}} = \left(\frac{B}{A}\right)^2, \quad (6)$$

where

$$A = \frac{\pi \epsilon_H R_{\text{XUV}}^3}{GM_p K_{\text{tide}}} \quad (7)$$

and

$$B = 2.248 \times 10^6 \left(\frac{R_p}{R_\oplus}\right)^{3/2} \text{ kg}^{1/2} \text{s}^{1/2}. \quad (8)$$

See Luger et al. (2015) for a derivation of these expressions.

In extreme cases, such as after a planet–planet scattering event (Rasio & Ford 1996; Lin & Ida 1997; Chatterjee et al. 2008), some planets may be so close to their star that the mass is stripped directly off the atmosphere by the stellar gravity. This process is typically called Roche lobe overflow. We model this process by assuming that mass is lost at the sound speed and call it “Bondi-limited escape”, following Owen & Wu (2016). If we assume the atmosphere to be composed exclusively of molecular hydrogen that behaves as an ideal gas, then the sound speed at the top of the atmosphere can be expressed as

$$c_s = \sqrt{\gamma k_b T_{\text{eff}} / m_H}, \quad (9)$$

where  $\gamma$  is 5/2 for an ideal gas,  $k_b$  is the Boltzmann constant, and  $T_{\text{eff}}$  is the effective temperature of the host star. Under these assumptions, we can recast Equation (4) of Owen & Wu (2016) as

$$\dot{M}_{\text{Bondi}} \approx 1.9 \times 10^{15} \left(\frac{M_p}{10M_\oplus}\right) \left(\frac{T_{\text{eff}}}{5800\text{K}}\right)^{1/2} \times \left(\frac{a}{0.1\text{au}}\right)^{1/4} \left(\frac{R_\odot}{R_*}\right)^{1/4} \text{ kg s}^{-1}, \quad (10)$$

where we leave this expression as an approximation due to the assumptions we made, but in practice we set the Bondi-limited mass rate to be equal to the right-hand side of this expression.

For our calculations we employ all three of these models (when applicable) and allow the software to change escape regimes as the star and planet evolve based on instantaneous conditions. In Figures 2 and 3, we present an example of how the mass loss evolves assuming a solar mass star orbited by a  $2M_\oplus$  planet that is half rock/half hydrogen by mass. The semimajor axis is 0.1 au, the eccentricity is 0, and  $\epsilon_H=0.1$ . Figure 2 shows the long-term evolution, while Figure 3 shows a zoom-in of the initial evolution of the envelope to highlight the Roche lobe overflow.

### 2.2.2. Water and Oxygen Loss

After the hydrogen envelope has been removed, the XUV photons can begin to dissociate the water molecules and drive more hydrogen escape and, in some cases, oxygen escape. We use the Bolmont et al. (2017) model for water escape as a function of  $F_{\text{XUV}}$  and refer the reader to Barnes et al. (2020) for more details on how this model is implemented in VPLanet. We also include two ways in which water behaves when planets reach the HZ: they either stop losing water or they do not (see Luger & Barnes 2015; Barnes et al. 2020; Becker et al. 2020).

The first case is a crude approximation of the setting of the conditions that allow the liquid water in the surface and avoid the catastrophic loss of water in the upper atmosphere (Wordsworth & Pierrehumbert 2013), and the second means planets are experiencing a runaway greenhouse. We use the “optimistic” HZ (Kopparapu et al. 2013) to determine when a planet is in the HZ.

### 2.3. Quiescent Stellar Evolution: STELLAR

The STELLAR module (Barnes et al. 2020) simulates the time evolution of stellar parameters such as the luminosity, radius, and effective temperature. This module interpolates the model grids of Baraffe et al. (2015) for stars between 0.08 and  $1.3 M_\odot$ . However, the Baraffe et al. (2015) grids do not include XUV evolution, which is poorly constrained for M-dwarf stars. Thus, we follow previous work and assume the empirical relationship obtained for solar-type stars (Ribas et al. 2005) applies to M dwarfs as well (see Luger & Barnes 2015; Fleming et al. 2020; Birky et al. 2021). In this model, the initial XUV luminosity remains a constant fraction of the bolometric luminosity for a duration called the “saturation time,” and afterwards the XUV fraction decays exponentially. See Barnes et al. (2020) for more details.

A critical piece of our analysis is the time a planet spends interior to the HZ. If we assume the “optimistic” interior HZ limit from Kopparapu et al. (2014) denotes the inner edge of the HZ, then Figure 4 shows the time a planet spends interior to the HZ as a function of host-star mass, assuming the planet is on a static, circular orbit. Planets orbiting  $0.2 M_\odot$  stars remain in the runaway greenhouse phase almost 4 times longer than those orbiting  $0.6 M_\odot$  stars and are therefore expected to lose more water and possess more oxygen-rich atmospheres. The smaller variations in the boundary are due to structural and temporal variations related to the onset (or not) of convection in the stellar interiors (Baraffe & Chabrier 2018). This result is consistent with Luger & Barnes (2015).

### 2.4. XUV Flare Evolution: FLARE

Here we present our new FLARE module for VPLanet. We first describe the mathematics of the model, followed by validation.

#### 2.4.1. Model Description

While the STELLAR module should capture most of the XUV luminosity of the star, it ignores the contribution from flares. Therefore, we have updated VPLanet to include a new module that estimates the time-averaged XUV luminosity due to stellar flares based on empirical data. In general, the XUV

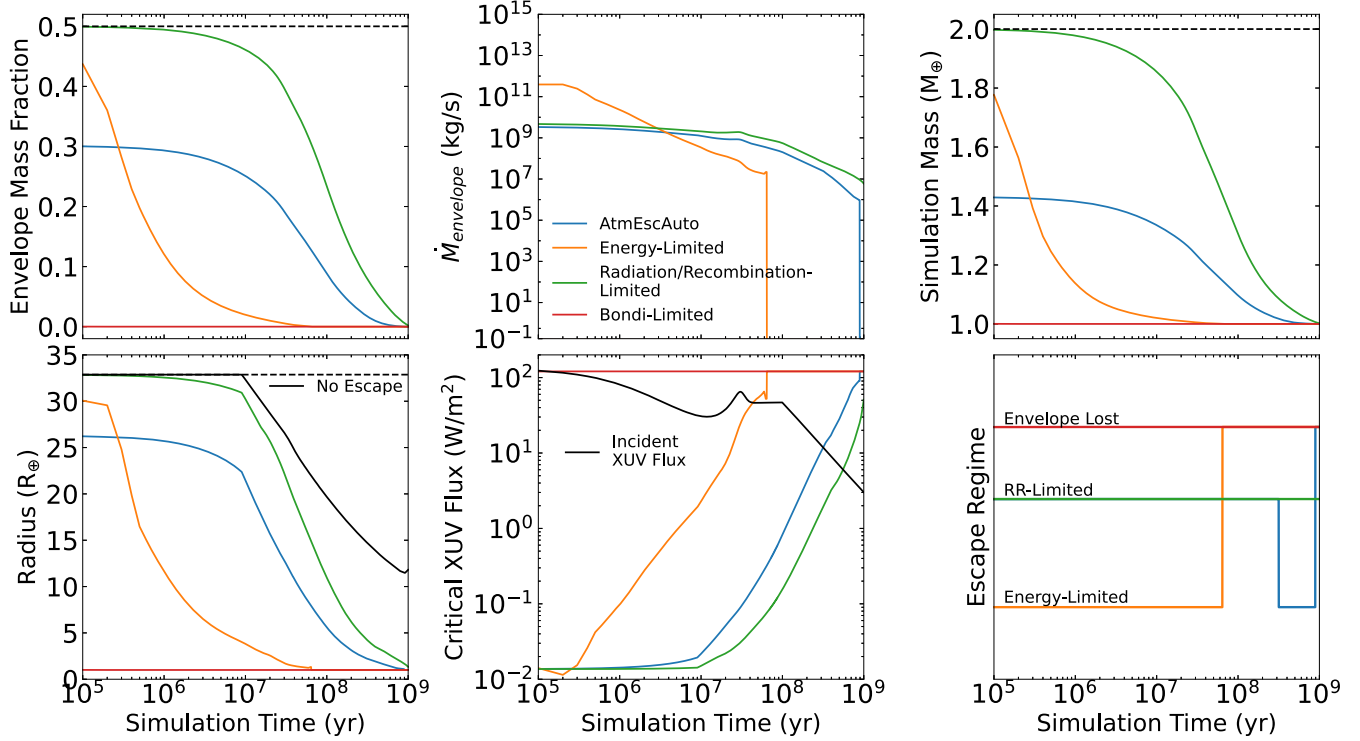


**Figure 2.** Examples of the evolution of a planet experiencing different types of envelope loss. In all panels, energy-limited escape is represented by orange, radiation/recombination-limited by green, Bondi-limited by red, and automatic “AtmEscAuto” by blue (the escape mechanism is determined by the instantaneous planetary and environmental conditions). Top left: fraction of the planet’s mass in the H envelope. Top center: time derivative of the envelope mass. Top right: total planet mass. Bottom left: planet radius. The “No Escape” curve (black) corresponds to a planet whose radius contracts as the planet cools, not due to atmospheric escape. Bottom center: critical XUV flux between energy-limited and radiation/recombination-limited escape. Bottom right: the H envelope escape “regime”. All planets start with the same initial conditions as described in the main text. The black dashed lines indicate the initial values for the respective quantities. [VPLanet/examples/AtmEscRegimes](#).

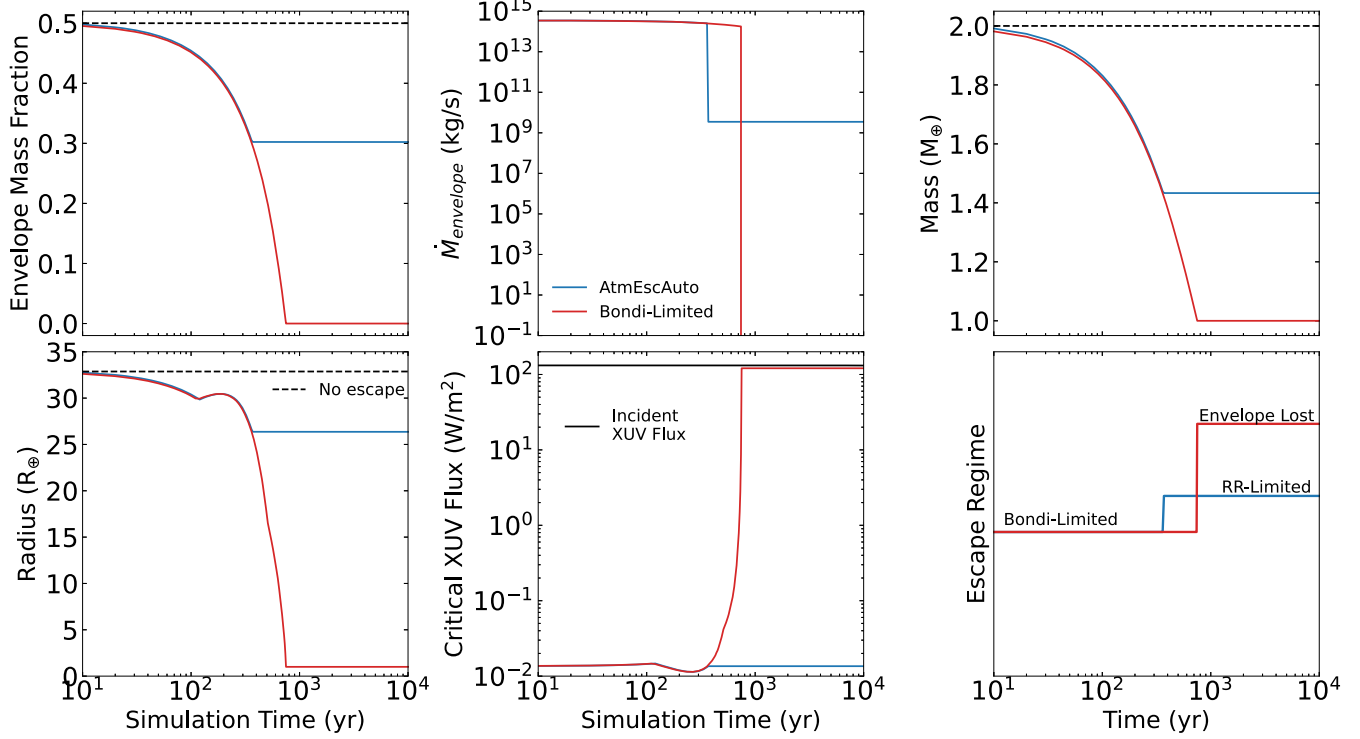


**Figure 3.** First 10,000 yr of atmospheric mass-loss for the Bondi-limited (red) and automatic cases (blue) with the same layout as Figure 2. Early on, the planetary radius exceeds the Roche limit and both planets experience immense mass loss of order 0.01 Earth masses per year! After about 300 yr, the radius has contracted to be less than the Roche limit, so the automatic model transitions from Bondi-limited escape to radiation/recombination-limited escape (the XUV flux is too large for energy-limited escape.) The Bondi-limited case, however, continues to lose massive amounts of H from its envelope, completely stripping the envelope within 1000 yr. [VPLanet/examples/AtmEscRegimes](#).

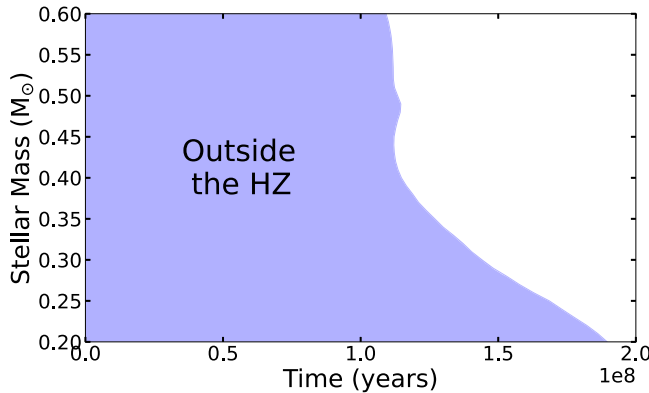


**Figure 4.** Duration of the runaway greenhouse phase (blue shadow region) for the hypothetical planets as a function of stellar mass assuming stellar evolution from Baraffe et al. (2015) and the optimistic HZ limits from Kopparapu et al. (2014). Plots/RGphase.

luminosity contribution by flares ( $L_{XUV,f}$ ) is given by

$$L_{XUV,f} = \int_{E_{\min}}^{E_{\max}} \nu(E_{XUV,f}) dE, \quad (11)$$

where  $E_{XUV,f}$  is the XUV energy of the flare, and  $\nu$  is the flare rate per unit energy.

To solve Equation (11), we must know the flare rate, which depends on both the age and stellar mass (see, e.g., West et al. 2008). We use the canonical relation from Lacy et al. (1976):

$$\log_{10}(\nu) = \alpha \log_{10}(E_{\text{Kepler}}) + \beta \quad (12)$$

with coefficients  $\alpha$  and  $\beta$  proposed by Davenport et al. (2019) based on flare observations in the Kepler field. The Davenport et al. (2019) model applies to active stars with masses between 0.2 and  $1.88 M_{\odot}$  and stellar flares with energies (in the Kepler bandpass) between  $10^{33}$  and  $10^{38}$  ergs. We convert the Kepler bandpass to XUV using the conversion factors from Osten & Wolk (2015, Table 2).

#### 2.4.2. Model Validation

To validate our model, we present the flare rate evolution as a function of the stellar age for a  $0.5 M_{\odot}$  star in Figure 5. This figure is indistinguishable from the top panel in Figure 10 from Davenport et al. (2019). Thus, we conclude that we have successfully incorporated this flare model into VPLanet.

Before moving on, we provide a few characteristics of the FLARE module. First, in Figure 6 we present two visualizations of how the flare frequency distribution (FFD) changes with time. The left panel shows the FFD for flares larger than the great AD Leo flare (Hawley & Pettersen 1991), whose energy in the Kepler bandpass  $E_{\text{kepler}}$  would have been approximately  $2.6 \times 10^{33}$  ergs.

This value was calculated using the information from Hawley & Pettersen (1991, Table 6A), where we take the flux integrated over the time interval at the UV bandpass (326–394 nm) equal to  $198 \times 10^{-8}$  ergs cm $^{-2}$ , and that divided by the flux integrated over the time interval in the continuum equal to  $1139 \times 10^{-8}$  ergs cm $^{-2}$ . Doing a quickly calculation, we have that the energy in the UV bandpass  $E_{UV}$  divided by the energy in the continuum  $E_{\text{continuum}}$  is equal to 0.174. From Hawley et al. (2014), we have that the ratio between  $E_{\text{Kepler}}$  and  $E_{UV}$  is 0.65. Rearranging, we have that  $E_{\text{Kepler}} = 0.174 / 0.65$

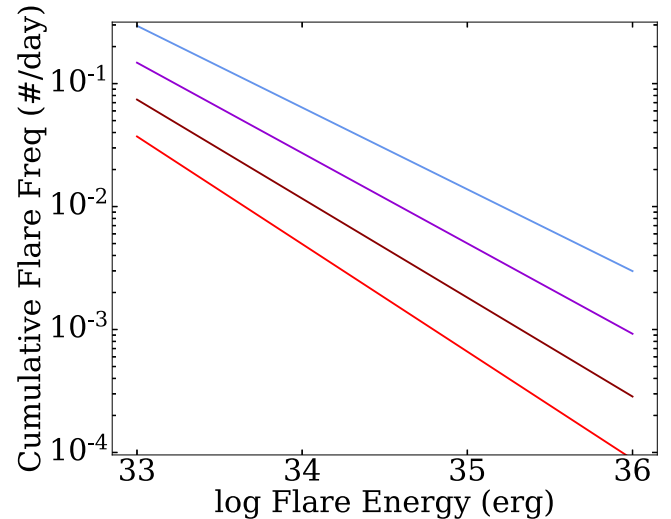


**Figure 5.** Reproduction of Figure 10 from Davenport et al. (2019) to validate the new FLARE module. The flare rate as a function of the flare energy for a  $0.5 M_{\odot}$  star is shown for ages of 1 Myr (blue), 10 Myr (purple), 100 Myr (brown), and 1 Gyr (red). Plots/MDwarfLuminosity/LumEvolFlareFFD.

$E_{\text{continuum}} = 0.26 E_{\text{continuum}}$ . This value agrees with the value found in Osten & Wolk (2015).

The Davenport et al. (2019) model predicts that planets orbiting early M dwarfs are more at risk of experiencing a flare of this magnitude than late M dwarfs. The right panel shows that the model predicts that less massive stars have a lower flare rate compared to more massive stars. This result seems to be inconsistent with other studies that find that flares from lower-mass stars are more powerful than those from larger stars (Hawley et al. 2014). This discrepancy may be due to the small number of M dwarfs in the Davenport (2016) catalog (<3% were M dwarfs) that formed the basis for the Davenport et al. (2019) model. Despite this apparent inconsistency, the Davenport et al. (2019) model is derived from the largest sample of M dwarfs currently available, so we will use it here but explicitly note that future work may need to replace this model with a more robust approximation for M-dwarf flaring.

Next we consider how flaring and quiescent evolution combine to modify the average XUV luminosity of stars as a function of the mass and age. We simulated five M-dwarf stars with masses between  $0.2$  and  $0.6 M_{\odot}$  using the STELLAR (Barnes et al. 2020) and FLARE modules (this work). As shown in Figure 7, including flares increases the XUV luminosity but generally not by more than 10% for any given star at a given time. We can see also that XUV luminosity by flares is more relevant to less massive stars after it enters the MS (see panels (e) and (f) of Figure 7). Also, panel (f) shows that the ratio between flare XUV and quiescent XUV increases with time. The quiescent XUV luminosity model we used comes from observational data of nonactive stars (Ribas et al. 2005), which show that quiescent XUV luminosity decreases with time. Hence as stars age, the XUV luminosity from flares becomes more important. The remaining panels provide additional depictions of the interplay of STELLAR and FLARE.

#### 2.5. Simulations

To estimate the influence of XUV from flares on the time evolution of the atmosphere and water content of Earth-like planets, we simulated hypothetical and known planets. We

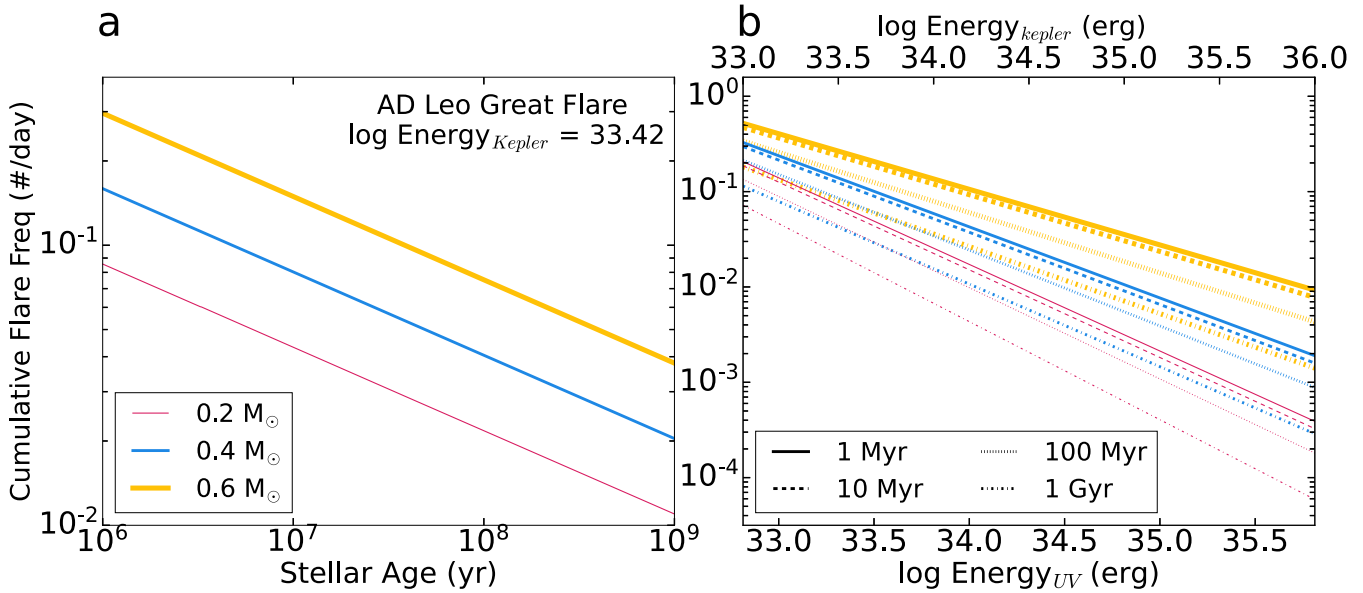


**Figure 6.** Flare frequency distribution predicted by the FLARE module. Panel (a) shows the FFD for flares with the energy of the AD Leo great flare (after converting the energy reported from Hawley & Pettersen (1991) to the Kepler bandpass) as a function of stellar age for three different stellar masses. Panel (b) shows the FFD for energies between  $10^{33}$  and  $10^{36}$  ergs for four different stellar ages [Plots/FfdMDwarfs](#).

assume the same atmospheric mass, thermosphere temperature, and absorption efficiency of XUV by hydrogen for all cases (see Tables 1 and 2). We consider flares with energies between  $10^{33}$  and  $10^{36}$  ergs, star masses between  $0.2$  and  $0.6 M_{\odot}$ , surface initial water content between 1 and 10 terrestrial oceans (TO), planets with a mass between  $0.5$  and  $5 M_{\oplus}$ , and hydrogen envelope masses of  $0.001 M_{\oplus}$ . For each parameter combination, we perform one simulation for which water loss is halted in the HZ and one for which it is not.

The hypothetical set represents a parameter sweep that explores the general trends that can occur over a plausible range of initial surface water content, planet mass, and host-star mass. The planet-star distance was selected to ensure that the planet would be interior to the HZ during the PMS of its host star and enter the HZ when the star is 1 Gyr old by combining the runaway greenhouse limit (Kopparapu et al. 2014, Equation (5)) with the predicted stellar properties at 1 Gyr from STELLAR. Furthermore, this synthetic group consisted of Earth-sized planets with the density of solids chosen from the Sotin et al. (2007) mass-radius relationship. The initial conditions for these simulations are presented in Table 1. In total, we simulated 25,160 scenarios.

In the second group, we simulated the known exoplanets Kepler-1229 b, K2-72 e, TOI-700 d, and Kepler-1649c, which have properties that are within the ranges of the hypothetical planets. We varied the water content and envelope mass but held fixed the values of the planetary and host-star masses, planetary radius, atmosphere temperature, and orbital parameters at their best-fit values. For the known planets, we only permit water loss prior to the planets reaching the HZ. For these planets we considered two distances: the reported semimajor axis for each planet (see Table 2) and one calculated with the same procedure as for the hypothetical planets. These two sets of simulations enable direct comparisons between the results with the hypothetical planets. The parameters for these simulations are summarized in Table 2, with values taken from the NASA Exoplanet Archive.

### 3. Results

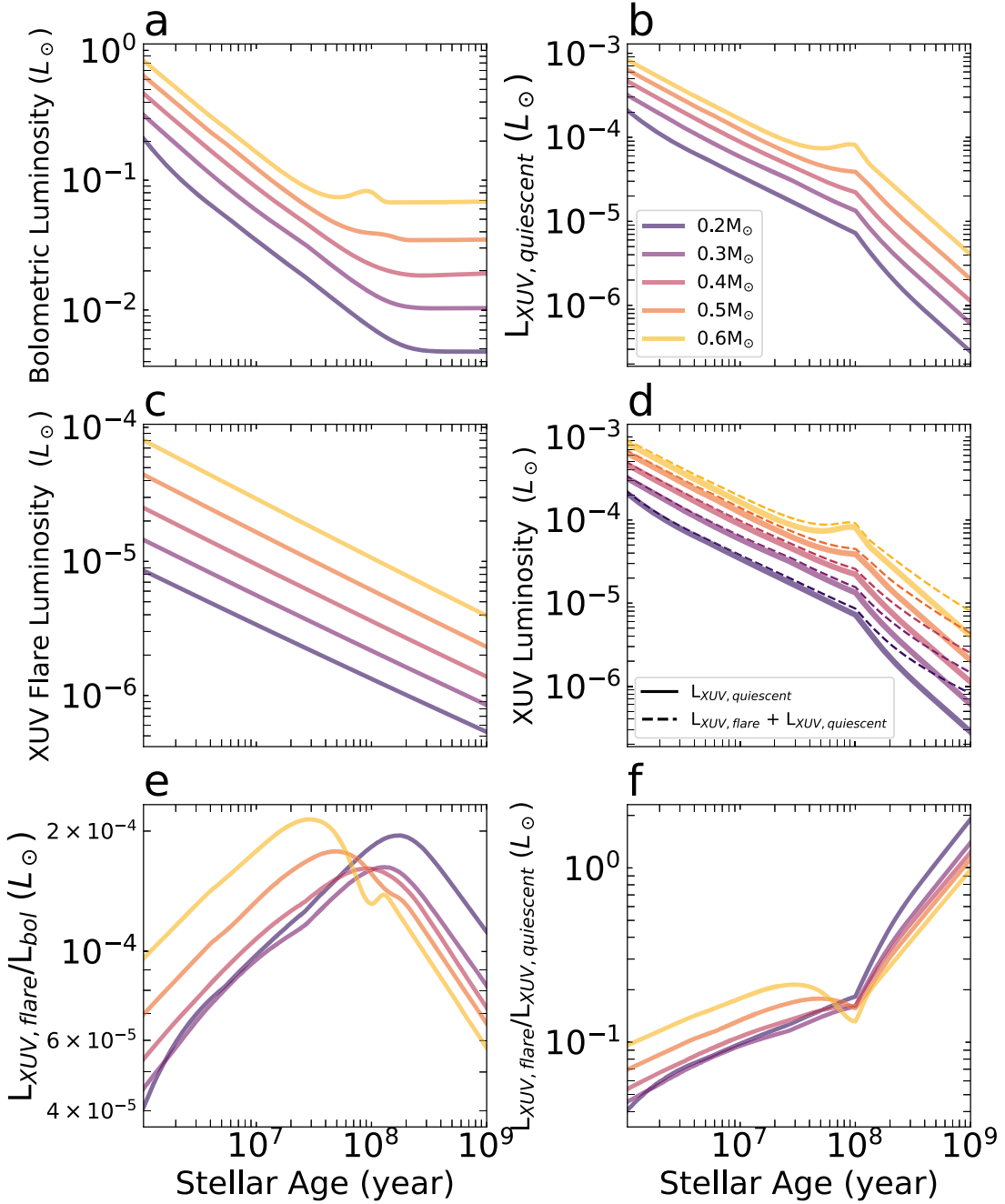
#### 3.1. Hypothetical Planets

Figure 8 shows the amount of water lost from the hypothetical planets for four assumptions: with/without flares (right/left columns) and with/without water loss in the HZ (lower/upper panels). The black lines represent the percentage of water lost with respect to the initial water content, and the symbols represent the approximate locations of the known planets discussed in Section 3.2. The amount of water lost is inversely proportional to the stellar and planetary mass in all four cases, but when flares are included, the amount of water lost increases by  $\sim 0.6$  TO when water is lost only in the HZ and by two TO when it is lost without restriction.

We find that water is only lost from massive planets when flares are included. This outcome is largely due to the more massive planets' ability to hold on to the hydrogen via their larger gravity. Without flares, the XUV flux is too low to drive significant mass loss, but flares provide enough XUV to drive additional loss, at least for the initial primordial envelope properties we assume here. We also find that the amount of water that escapes is independent of the initial water abundance.

To quantify the role of flares, we subtract the water loss from simulations that include flares from those that do not. Figure 9 shows the results and includes both relative (contours) and absolute (colors) mass loss amounts. The top panels of Figure 9 include water loss in the HZ, while the bottom panels do not. The first feature to note is that flares can remove up to two additional TO, a total desiccation of the surface water in some cases. When flares are not included, less water escapes from more massive planets orbiting more massive stars. On the other hand, cases with a shorter runaway greenhouse phase (bottom panels from Figure 9) or planets equal to or less massive than  $2 M_{\oplus}$  can only lose up to 36% more water due to flares.

The biggest difference occurs for  $\sim 3 M_{\oplus}$  planets orbiting stars less massive than  $0.3 M_{\odot}$ , as shown in Figure 9. For the case with a runaway greenhouse in the HZ, the planets can lose



**Figure 7.** Stellar evolution with and without flaring for stellar masses between  $0.2 M_{\odot}$  and  $0.6 M_{\odot}$ . Panels (a) and (b) show the bolometric luminosity and XUV quiescent luminosity, respectively, while panels (c) and (d) show the XUV luminosity from flares and the total XUV luminosity with (dashed lines, i.e., the sum of parameters from panel (b) and (c)) and without (continuous lines) flares, respectively. Panel (e) shows the ratio between XUV luminosity from flares and bolometric luminosity, and panel (f) shows the ratio between XUV luminosity from flares and XUV quiescent luminosity. The colors represents different stellar mass as labeled in the legend. [Plots/MDwarfLuminosity/LumEvolStellar](#).

up to an additional 0.6 TO of water than cases that not consider flares (a 44% increase). For the cases where planets have a shorter period in the runaway greenhouse, i.e., only during PMS, the flares can remove up to two TO, or 100% of the surface water.

Note that for planets with small initial water content, the inclusion of flares does not affect water-loss rates because the quiescent XUV flux is sufficient for desiccation. In other words, these planets lose all their hydrogen and water regardless of stellar activity. In general, potentially habitable planets must form with at least four TO of water to be habitable

after the PMS. With this value, the planets can keep (in a general way) approximately 50% of the amount of water they have at the beginning of their evolution.

Next we turn to the accumulation of the liberated oxygen in the atmosphere due to flares. In Figure 10, we plot the difference in final oxygen abundance between atmospheres that are exposed to flares versus those that are not in an analogous manner to Figure 9. The white regions of this figure are the cases where the oxygen produced by flares is equal to the quiescent case; red regions (positive values) show additional

**Table 1**  
Parameters for the Hypothetical Cases

Parameter	Value
Planet mass( $M_{\oplus}$ )	[0.5–5, 0.5]
Planet density ( $\text{g cm}^{-3}$ )	4.85–7.54
Envelope mass( $M_{\oplus}$ )	1.0E-3
Surface water mass (TO)	[1–10, 0.25]
XUV water escape efficiency	Bolmont et al. (2017)
XUV hydrogen escape efficiency	0.15
Thermosphere temperature (K)	400
Semi-axis major <sup>a</sup> (AU)	[0.07306–0.283186]
Stellar mass( $M_{\odot}$ )	[0.2–0.6, 0.025]
Saturated XUV luminosity fraction	1.0E-3
XUV saturation time (Myr)	100
Initial stellar age (Myr)	1
Flare energy (ergs)	1.0E33–1.0E36
Simulation time (Myr)	1.0E3
Time step <sup>b</sup> (yr)	~0.4–~1.6E3
VPLanet modules	AtmEsc, STELLAR, FLARE

**Notes.**

<sup>a</sup> Calculated using  $1.053 \times$  the distance of the inner limit of the HZ for runaway greenhouse from (Kopparapu et al. 2014, Equation (5)).

<sup>b</sup> Dynamically selected during the simulation.

oxygen accumulation from flares; blue regions (negative values) show reduced oxygen abundance.

Flares can generate up to 95 and 318 bars of additional oxygen when water photolysis is halted in the HZ and when it is not, respectively. The blue regions do not represent cases in which less oxygen was produced, but rather where the XUV flux drives a more energetic flow of hydrogen that is able to drag along more oxygen. This effect can be seen by noting that

the blue region overlaps with the fully desiccated regions of Figure 9, revealing that similar amounts of oxygen are produced but more oxygen escapes, resulting in less oxygen in the atmosphere at the conclusion of the simulations.

Even though we did not consider an oxygen sink in this work, we note that in a real Earth-like planet, the atmospheric oxygen can be removed in different ways, like metamorphism, weathering, and volcanism (Catling & Kasting 2017). As seen recently in previously works (Schaefer et al. 2016; Wordsworth et al. 2018; Barth et al. 2021), a magma ocean can also absorb oxygen efficiently. Nonetheless, all these studies still suggest that significant oxygen can accumulate in the atmosphere.

### 3.2. Known Planets

Next we turn to the four real planets we selected in Section 2.4.2. For these simulations we assume that once a planet reaches the HZ, the water loss is halted. Figure 11 shows the positions of these planets in the HZ. Figure 12 shows the time evolution of primordial envelope mass, surface water content, amount of atmospheric oxygen, optimistic HZ and semimajor axis, XUV-to-bolometric luminosity ratio, and incident XUV flux for each planet. In the top panels of both figures, this location is an extrapolation, once we did not simulate scenarios with an extended runaway greenhouse phase.

The simulations reveal that K2-72 e can lose its entire primordial H/He atmosphere when flares are included, regardless of the distance from the star. However, this planet does not lose any water because it enters the HZ just before it loses all its primordial H/He atmosphere. About 600 Myr after the scenario with flares, the analog scenario with the quiescent XUV only also loses its primordial atmosphere.

**Table 2**  
Parameters used to Simulate the Final Water Content in the Simulations of Known Planets

Parameter	Kepler-1229 b	K2-72 e	TOI-700 d	Kepler-1649 c
Planet mass <sup>a</sup> ( $M_{\oplus}$ )	2.93	2.55	1.63984	1.2389
Planet radius ( $R_{\oplus}$ )	1.34	1.29	1.144	1.06
Planet density ( $\text{g cm}^{-3}$ )	6.69	6.52	6.018	5.715
Envelope mass ( $M_{\oplus}$ )	1.0E-3	1.0E-3	1.0E-3	1.0E-3
Surface water (TO)	1,10	1,10	1,10	1,10
XUV water escape efficiency	(Bolmont et al. 2017)	(Bolmont et al. 2017)	(Bolmont et al. 2017)	(Bolmont et al. 2017)
XUV hydrogen escape efficiency	0.15	0.15	0.15	0.15
Thermosphere temperature (K)	400	400	400	400
Actual semimajor axis (AU)	0.3006	0.106	0.1633	0.0827
Modified semimajor axis <sup>b</sup> (AU)	0.19685	0.102468	0.16247	0.07643
Eccentricity	0.11	0	0.111	0
Stellar mass ( $M_{\odot}$ )	0.480	0.271365	0.415	0.1977
Saturated XUV luminosity fraction	1.0E-3	1.0E-3	1.0E-3	1.0E-3
XUV saturation time (Myr)	100	100	100	100
Initial stellar age (Myr)	1	1	1	1
Flare energy (ergs)	11.0E33–1.0E36	1.0E33–1.0E36	1.0E33–1.0E36	1.0E33–1.0E36
Simulation time (Myr)	1.0E3	1.0E3	1.0E3	1.0E3
Time step <sup>c</sup> (yr)	~4.8E-2–1.0E4	~6E-2–1.0E4	~5E-2–1.0E4	~6E-2–1.0E4
VPLanet modules	AtmEsc, STELLAR, FLARE	AtmEsc, STELLAR, FLARE	AtmEsc, STELLAR, FLARE	AtmEsc, STELLAR, FLARE
Source (planetary radius, stellar mass and semimajor axis)	Torres et al.(2017)	Dressing et al.(2017)	Rodriguez et al.(2020)	Vanderburg et al. (2020)

**Notes.**

<sup>a</sup> The masses are calculated with the Sotin et al. (2007) model for terrestrial planets.

<sup>b</sup> Calculated using  $1.053 \times$  the distance of the inner limit of the HZ for runaway greenhouse from Kopparapu et al. (2014, Equation (5)).

<sup>c</sup> Dynamically selected during the simulation.

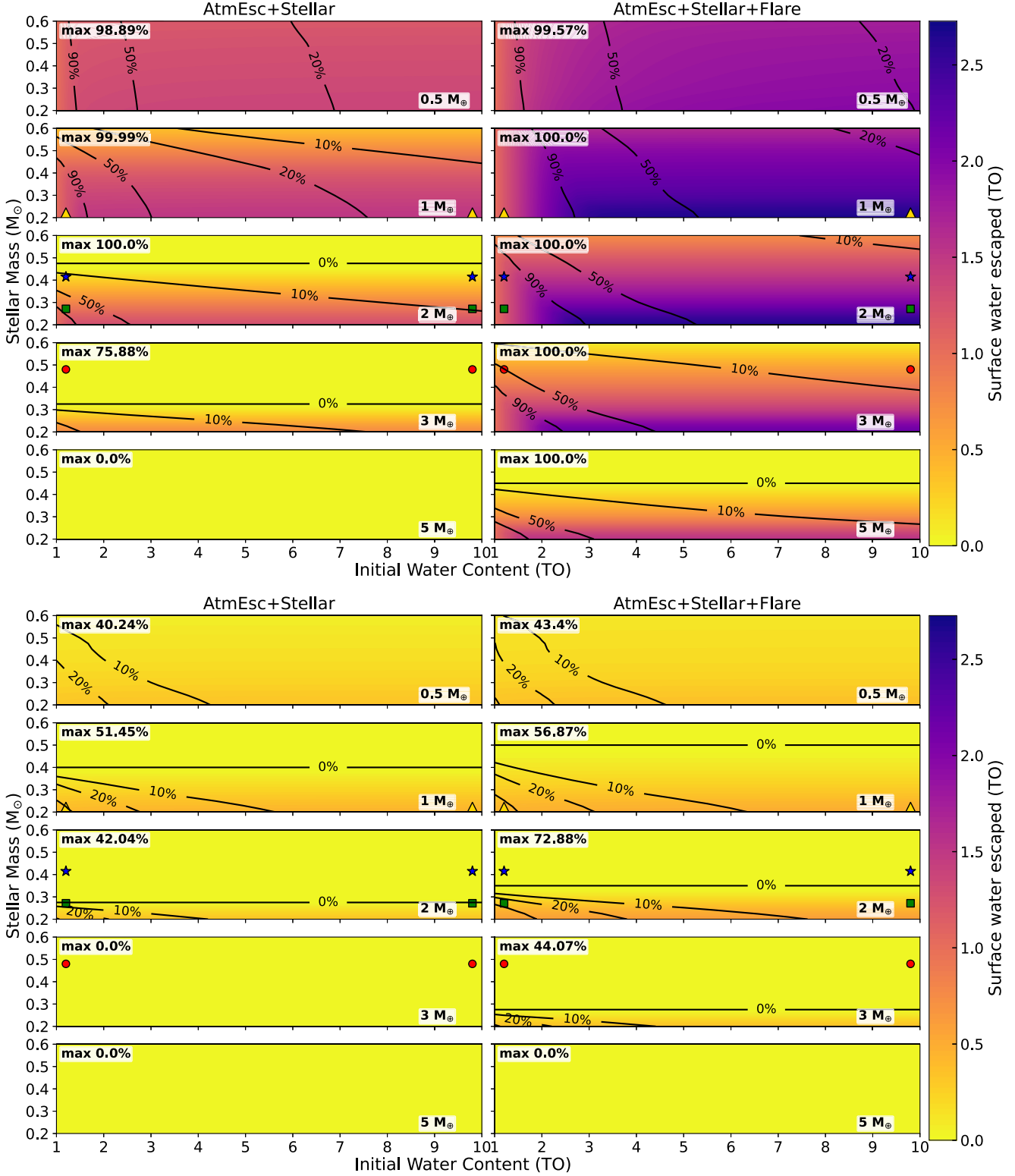


**Figure 8.** Percentage (contour lines) and absolute amount (shading) of water lost just by quiescent stellar XUV (AtmEsc + Stellar modules; left panels) and with the addition of flares (AtmEsc + Stellar + Flare modules; right panels). In the upper panels, the planet continues to lose water even when in the HZ, while in the lower panels, water photolysis halts in the HZ. The circle, square, star, and triangle represent Kepler-1229 b, K2-72 e, TOI-700 d, and Kepler-1649c, respectively; see Table 2. Plots/SurfaceWaterEscape/WaterEscapeAbsolute.

The Kepler-1649c planet is the only one of these four simulated planets that loses water. Unlike K2-72 e, in Kepler-1649c this process happens when the planet is placed closer to the star, with its known semimajor axis, regardless of flaring.

The only difference is that, with flares, the primordial atmosphere escapes 30 Myr earlier.

Planet Kepler-1229 b does not lose its envelope even when flares are included, mostly due to its larger mass that helps to retain the hydrogen. TOI-700 d, even with less mass than K2-

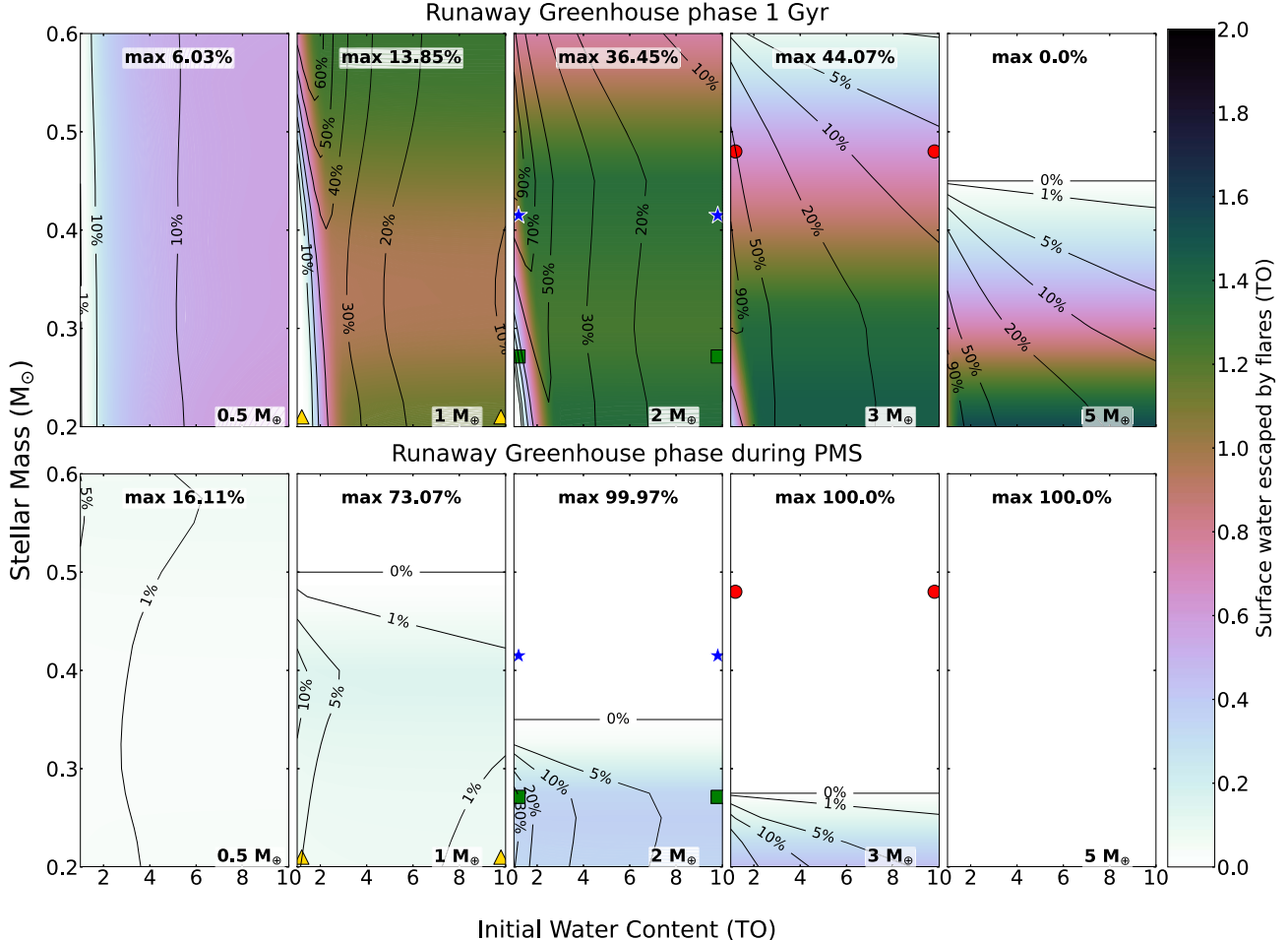


**Figure 9.** Flare only contribution to the water lost in percentage (contour lines) and absolute amount (shades) in TO, i.e., right panels minus left panels from Figure 8. In the top panels, the runaway greenhouse phase occurs throughout all the simulation. In the bottom panels, the runaway greenhouse effect stops when the planet enters the (optimistic) habitable zone. [Plots/SurfaceWaterEscape](#).

72 e, does not lose its primordial envelope either, and in this case, the larger orbital distance from the star further helps to prevent the atmospheric loss. All these results are in agreement with the hypothetical cases (see Figures 8, 9, and, 10), and confirm that the impact of flaring on envelope loss and desiccation depend strongly on the specific properties of a given planet.

#### 4. Discussion

##### 4.1. Dependence of the Stellar and Planetary Mass to the Final Water Reservoir

After carrying out the simulations with the parameters shown in Table 1, the values of the final amounts of water were taken for each simulated planet. With these data, the percentage of the water lost (compared to the initial value) was also calculated for each planet.

The hypothetical planets simulated in this work suggest strong correlations between stellar+planetary parameters and final water content. To quantify these relationships, we performed a Pearson's correlation test on those data. The Pearson correlation assumes linear dependency on pair of parameters. To use this test, we considered that the data are linearly correlated. The Pearson's coefficient varies from  $-1$  (perfectly anticorrelated) to  $1$  (perfectly correlated). A Pearson coefficient equal to zero means that the data sets are

uncorrelated. Figure 13 shows the results of this analysis with respect to the percentage of surface water, for the four scenarios (water loss in the HZ and the inclusion of flares). Panels (b) and (d) include flares; panels (c) and (d<sub>+</sub>) assume the planets do not lose water in the HZ (the runaway greenhouse phase occurs only during the PMS).

In all cases, the Pearson test confirms that stellar and planetary masses are inversely correlated with the amount of water lost, i.e., less massive stars play a major role in water loss. Although more massive stars have larger flare rates in our model, their PMS phase is shorter and thus less water is lost. For the scenario where we consider flares (panels (b) and (d) of Figure 13), the correlation between atmospheric loss with stellar mass increases compared to the cases without flares. When we assumed that the planet remains in a runaway greenhouse phase throughout 1 Gyr (panels (a) and (b) of Figure 13), the correlation between final water abundance and stellar mass decreases compared to planet mass because water loss is independent of the duration of the PMS.

More massive planets possess stronger gravity and retain their atmosphere and water more easily than less massive planets, especially when the planet stays in the runaway greenhouse phase for 1 Gyr. If just the quiescent XUV of the star is considered, the correlation value is  $-0.58$ . When we add flares to the stellar evolution, the correlation drops to a value of  $-0.47$ .

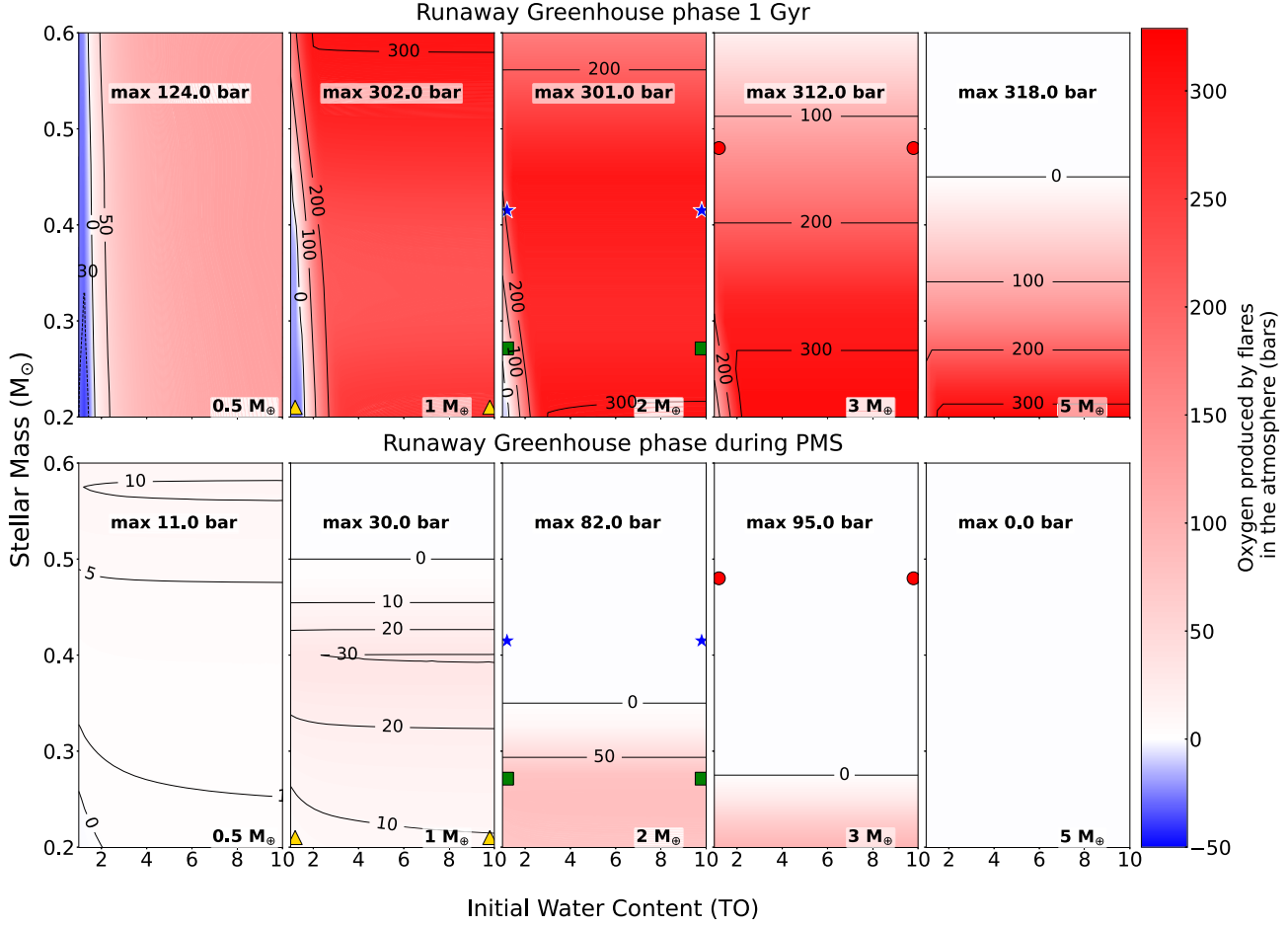


**Figure 10.** Amount of oxygen produced by flares (effect of FLARE module) in the same format as Figure 9 but with different colors as shown in the color bar. Plots/[OxygenBuildUp](#).

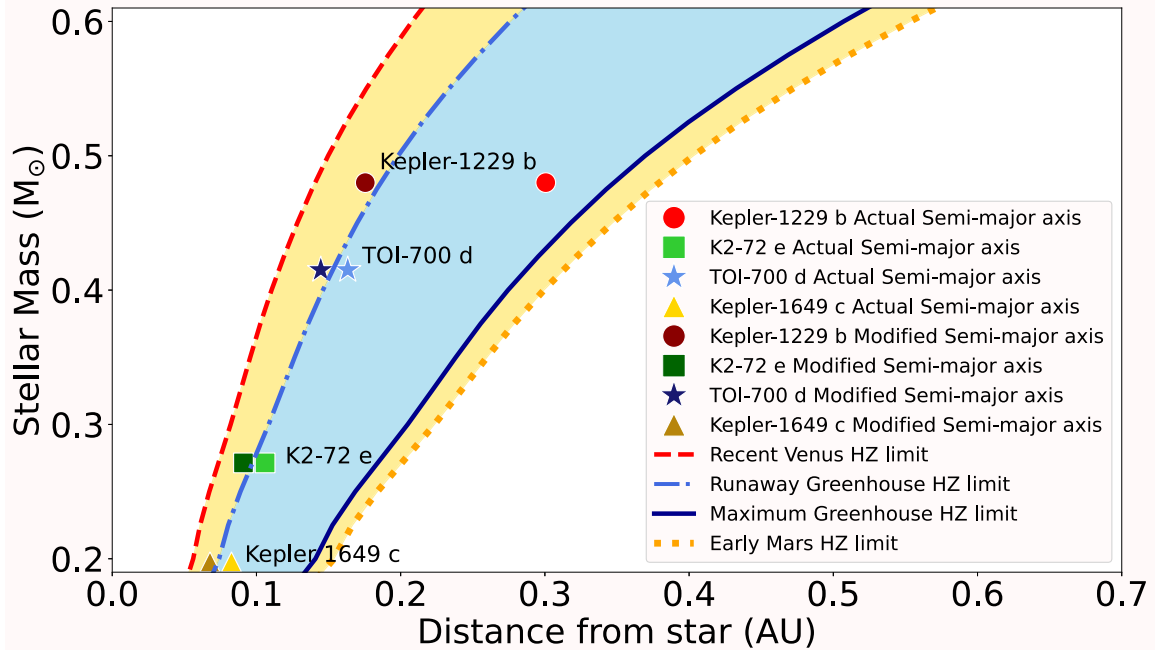


**Figure 11.** Position of known planets with respect to the host star. The blue shading represents the conservative HZ, and the region between the red (dashed) and orange (dotted) lines are the optimistic HZ, as defined by Kopparapu et al. (2014). The known planets are represented as circles (Kepler-1229 b), squares (K2-72 e), stars (TOI-700 d), and triangles (Kepler-1649 c). Plots/[RealPlanets](#)/[RealPlanetsPosition](#).

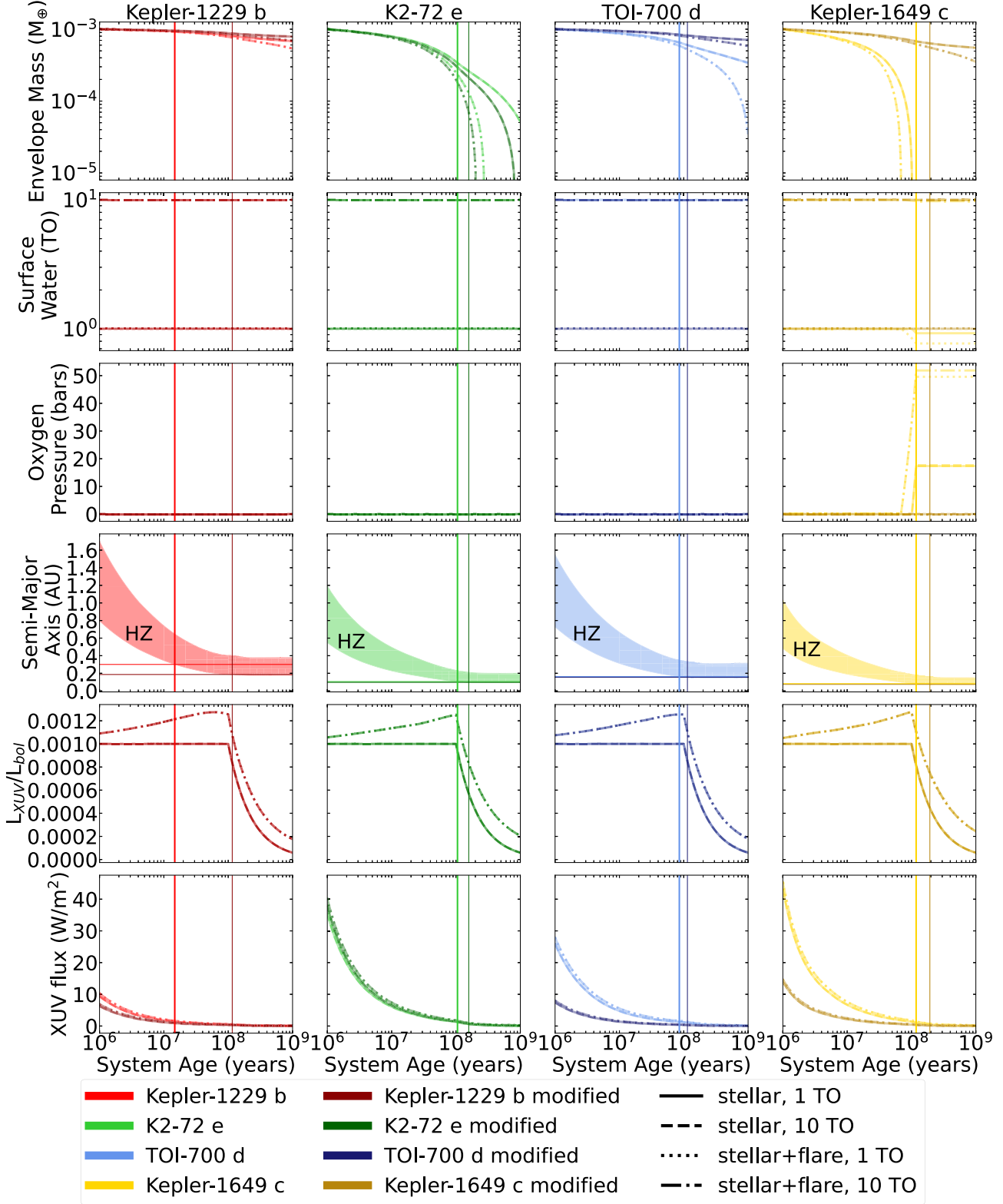


**Figure 12.** Time evolution of planetary parameters for the known planets. From top to bottom: atmospheric mass, surface water, atmospheric oxygen, habitable zone position with respect to the host star, XUV and bolometric luminosity ratio, and XUV flux incoming the planet. [Plots/RealPlanets/RealPlanetsSimulation](#).

This stellar mass trend depends on the length of the runaway greenhouse phase. When the runaway greenhouse phase is the same for all the stellar masses (panels (a) and (b)), the dependence on the stellar mass is weaker than when the runaway greenhouse halts when the planet enters the HZ

(panels (c) and (d)). Here the water lost depends on planetary mass almost equally ( $-0.4$  and  $-0.38$ , respectively), but the stellar mass is more relevant when we consider flares (see panel (d)). In this case, the Pearson coefficient is  $-0.41$  (panel (d)),

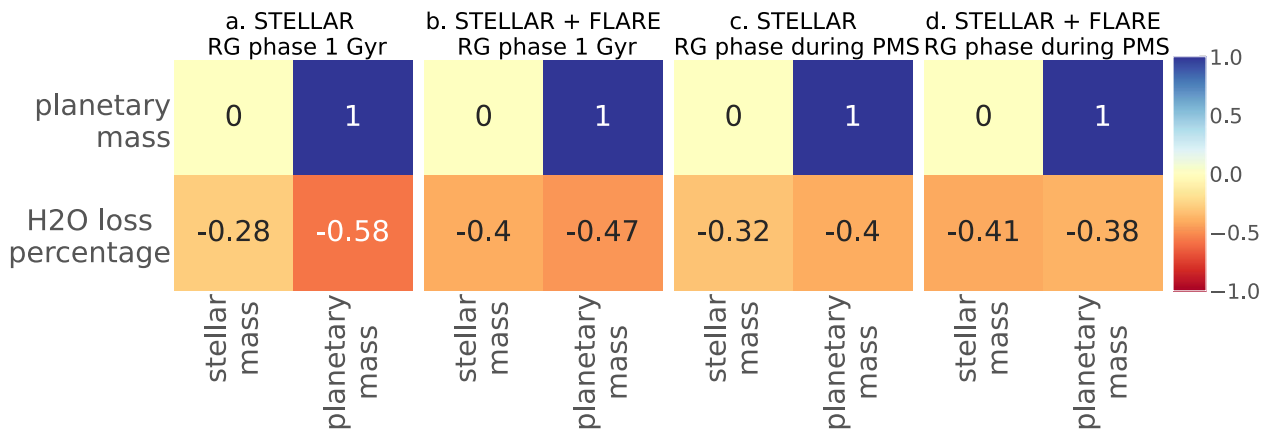


**Figure 13.** Pearson correlation coefficient for final water mass for four different assumptions. Panel (a) assumes the planets lose water in the HZ and does not include flares. Panel (b) also assumes the planets lose water in the HZ but that the host-star flares. Panels (c) and (d) assume water loss halts in the HZ, with panel (c) excluding flares and panel (d) including them. [Plots/Correlation](#).

compared to a value of  $-0.32$  when we do not consider flares (panel (c)).

Finally, we note that the flare model from Davenport et al. (2019) contains uncertainties that are not reflected in this analysis. In that work, the authors only considered a few M-dwarf stars in their sample, the observed flares have high energies ( $>31.5$  ergs), and their analyzed stars are all active. These limitations likely make our results an upper limit of the simulated scenarios. Future flare observations of M dwarfs (e.g., achieved with the Transiting Exoplanet Survey) will likely require modifications of the FFD as a function of stellar mass and time. When such an effort has been completed, the results presented here should be revisited.

#### 4.2. Impact of Flares on Known Planets

Our simulations of known planets revealed a wide range of plausible evolutionary trajectories; however, the range is likely underestimated. We assumed that the planets orbit active stars, but that is probably not the case for many of them. TOI-700 is a slow rotator (period = 54 days; Newton et al. 2017; Gilbert et al. 2020; Rodriguez et al. 2020), indicating this star is not currently active. Kepler-1229 has a rotation period of 17.63 days (Torres et al. 2017), so it could be active, but like K2-72 and Kepler-1649, it has no activity or flares reported in the literature. However, these observations are all for their current conditions and, since stellar activity decreases with time (West et al. 2008), our simulations may still be representative of their early evolution. Otherwise, the results presented here can be considered an upper limit (worst case) of the environment that these planets are exposed to.

Cohen et al. (2020) found that TOI-700 d is not in an extreme environment compared to Earth, even considering a strong coronal mass ejection (CME) event. Dong et al. (2020) found that the planet's atmosphere could be stripped within 1 Gyr if the planet is unmagnetized. This result is consistent with our study, as shown in Figure 12. If we extrapolate the results, TOI-700 d's envelope mass could be lost just after 1 Gyr. Note, however, that our simulations also predict that water can be retained, even when considering flares. Even with flares, the only case that experienced significant water lost was Kepler-1649c, removing 0.16 TO more than quiescent evolution alone. This result is likely due to the short orbital distance

and small stellar mass, which increase the time the planet is interior to the HZ.

## 5. Conclusions

We simulated the XUV emission of M-dwarf stars to estimate the atmospheric escape and oxygen buildup on synthetic and known Earth-size planets. For the first set of simulations, we modeled a range of parameters, such as the stellar mass, planetary mass, and initial water abundance, to estimate the trajectories that permit water on the planetary surfaces today, i.e., a habitable planet. We find that many planets, including some that are known, could be habitable today. However, we also note that other processes can affect habitability, such as tidal forces, planetary magnetic field, CMEs, or proton events. We also did not consider radiative cooling mechanisms, such as from CO<sub>2</sub>, in the simulated atmospheres. These are important features to the atmospheric escape when we are analyzing planetary habitability but are beyond the scope of this work and should be explored with future research. Because of all these points, our results should be considered preliminary, especially for the known planets.

As part of this work, we added the Davenport et al. (2019) flare frequency distribution model to the VPLanet software package as a module we call FLARE. We validated this model by reproducing the results in Davenport et al. (2019). This module is now part of this open-source project and available for community use.

We found that flares add about 10% more XUV emission to M dwarfs over the quiescent stellar levels, which can remove up to an additional two TO of surface water compared to quiescent stars, at least for Earth-like planets. We assumed a primordial hydrogen envelope mass of  $0.001 M_{\oplus}$ , so actual water amounts lost will change for different envelope assumptions. We also found that flares play their most significant role in water escape for planets between 2 and  $5 M_{\oplus}$ . Furthermore, the final water content depends more strongly on the stellar mass than the planetary mass when water loss halts once the planet reaches the HZ. However, if the planets continue losing water inside the HZ, then planetary mass is more important. These trends hold for our simulations of known planets. Future space missions such as the James Webb Space Telescope and the ground-based Extremely Large Telescope may be able to test the predictions presented here,

possibly even leading to the discovery of an inhabited exoplanet.

R.B. acknowledges support from NASA grants 80NSSC20K0229 and the NASA Virtual Planetary Laboratory Team through grant No. 80NSSC18K0829. L.N.R.A. and A.S. acknowledge the support of UNAM DGAPA PAPIIT project IN110420. LNRA thanks CONACYT's graduate scholarship program for its support. We thank David Fleming for developing the automatic mass-loss functionality and Caitlyn Wilhelm for developing vspace and the multiplanet codes that facilitated our parameter sweeps.

*Facility:* Exoplanet Archive.

*Software:* VPLanet (Barnes et al. 2020).

## ORCID iDs

- Laura N. R. do Amaral <https://orcid.org/0000-0002-8341-0376>  
 Rory Barnes <https://orcid.org/0000-0001-6487-5445>  
 Antígona Segura <https://orcid.org/0000-0002-2240-2452>  
 Rodrigo Luger <https://orcid.org/0000-0002-0296-3826>

## References

- Atri, D., & Mogan, S. R. C. 2021, *MNRAS*, **500**, L1  
 Audard, M., Güdel, M., Drake, J. J., & Kashyap, V. L. 2000, *ApJ*, **541**, 396  
 Baraffe, I., & Chabrier, G. 2018, *A&A*, **619**, A177  
 Baraffe, I., Chabrier, G., Allard, F., & Hauschildt, P. 1998, *A&A*, **337**, 403  
 Baraffe, I., Homeier, D., Allard, F., & Chabrier, G. 2015, *A&A*, **577**, A42  
 Barnes, R., Mullins, K., Goldblatt, C., et al. 2013, *AsBio*, **13**, 225  
 Barnes, R., Deitrick, R., Luger, R., et al. 2016, arXiv:1608.06919  
 Barnes, R., Luger, R., Deitrick, R., et al. 2020, *PASP*, **132**, 024502  
 Barth, P., Carone, L., Barnes, R., et al. 2021, *AsBio*, **21**, 1325  
 Becker, J., Gallo, E., Hodges-Kluck, E., Adams, F. C., & Barnes, R. 2020, *AJ*, **159**, 275  
 Billings, L. 2011, *Nature News*, **470**, 27  
 Birkby, J., Barnes, R., & Fleming, D. P. 2021, *RNAAS*, **5**, 122  
 Bochanski, J. J., Hawley, S. L., Covey, K. R., et al. 2010, *AJ*, **139**, 2679  
 Bolmont, E., Selsis, F., Owen, J. E., et al. 2017, *MNRAS*, **464**, 3728  
 Catling, D. C., & Kasting, J. F. 2017, *Atmospheric Evolution on Inhabited and Lifeless Worlds* (Cambridge: Cambridge Univ. Press)  
 Chatterjee, S., Ford, E. B., Matsumura, S., & Rasio, F. A. 2008, *ApJ*, **686**, 580  
 Cockell, C. S., Bush, T., Bryce, C., et al. 2016, *AsBio*, **16**, 89  
 Cohen, O., Garraffo, C., Moschou, S.-P., et al. 2020, *ApJ*, **897**, 101  
 Davenport, J. R. 2016, *ApJ*, **829**, 23  
 Davenport, J. R., Covey, K. R., Clarke, R. W., et al. 2019, *ApJ*, **871**, 241  
 Dole, S. H. 1964, *Habitable Planets for Man* (Santa Monica, CA: Rand Corporation)  
 Dong, C., Jin, M., & Lingam, M. 2020, *ApJL*, **896**, L24  
 Dotter, A., Chaboyer, B., Jevremović, D., et al. 2008, *ApJS*, **178**, 89  
 Dressing, C. D., Vanderburg, A., Schlieder, J. E., et al. 2017, *AJ*, **154**, 207  
 Duvvuri, G. M., Pineda, J. S., Berta-Thompson, Z. K., et al. 2021, *ApJ*, **913**, 40  
 Erkaev, N. V., Kulikov, Y. N., Lammer, H., et al. 2007, *A&A*, **472**, 329  
 Estrela, R., Palit, S., & Valio, A. 2020, *AsBio*, **20**, 1465  
 Fleming, D. P., Barnes, R., Luger, R., & VanderPlas, J. T. 2020, *ApJ*, **891**, 155  
 Fontenla, J. M., Linsky, J. L., Witbrod, J., et al. 2016, *ApJ*, **830**, 154  
 France, K., Fleming, B. T., Drake, J. J., et al. 2019, *Proc. SPIE*, **11118**, 1111808  
 France, K., Duvvuri, G., Egan, H., et al. 2020, *AJ*, **160**, 237  
 Fujii, Y., Angerhausen, D., Deitrick, R., et al. 2018, *AsBio*, **18**, 739  
 Garrett, D., Savransky, D., & Belikov, R. 2018, *PASP*, **130**, 114403  
 Gilbert, E. A., Barclay, T., Schlieder, J. E., et al. 2020, *AJ*, **160**, 116  
 Hawley, S. L., Davenport, J. R., Kowalski, A. F., et al. 2014, *ApJ*, **797**, 121  
 Hawley, S. L., & Pettersen, B. R. 1991, *ApJ*, **378**, 725  
 Hayashi, C. 1966, *ARA&A*, **4**, 171  
 Hunten, D. M., Pepin, R. O., & Walker, J. C. G. 1987, *Icar*, **69**, 532  
 Kasting, J. F. 1988, *Icar*, **74**, 472  
 Kasting, J. F., Whitmire, D. P., & Reynolds, R. T. 1993, *Icar*, **101**, 108  
 Kopparapu, R. K. 2013, *ApJL*, **767**, L8  
 Kopparapu, R. K., Ramirez, R. M., SchottelKotte, J., et al. 2014, *ApJL*, **787**, L29  
 Kopparapu, R. K., Ramirez, R., Kasting, J. F., et al. 2013, *ApJ*, **765**, 131  
 Lacy, C. H., Moffett, T. J., & Evans, D. S. 1976, *ApJS*, **30**, 85  
 Laughlin, G., Bodenheimer, P., & Adams, F. C. 1997, *ApJ*, **482**, 420  
 Lin, D. N. C., & Ida, S. 1997, *ApJ*, **477**, 781  
 Linsky, J. L., Fontenla, J., & France, K. 2013, *ApJ*, **780**, 61  
 Lopez, E. D., Fortney, J. J., & Miller, N. 2012, *ApJ*, **761**, 59  
 Luger, R., & Barnes, R. 2015, *AsBio*, **15**, 119  
 Luger, R., Barnes, R., Lopez, E., et al. 2015, *AsBio*, **15**, 57  
 Murray-Clay, R. A., Chiang, E. I., & Murray, N. 2009, *ApJ*, **693**, 23  
 Newton, E. R., Irwin, J., Charbonneau, D., et al. 2017, *ApJ*, **834**, 85  
 Osten, R. A., & Wolk, S. J. 2015, *ApJ*, **809**, 79  
 Owen, J. E., & Wu, Y. 2016, *ApJ*, **817**, 107  
 Peacock, S., Barman, T., Shkolnik, E. L., et al. 2020, *ApJ*, **895**, 5  
 Ramirez, R. M., & Kaltenegger, L. 2014, *ApJL*, **797**, L25  
 Rasio, F. A., & Ford, E. B. 1996, *Sci*, **274**, 954  
 Ribas, I., Guinan, E. F., Güdel, M., & Audard, M. 2005, *ApJ*, **622**, 680  
 Rodriguez, J. E., Vanderburg, A., Zieba, S., et al. 2020, *AJ*, **160**, 117  
 Salz, M., Schneider, P. C., Czesla, S., & Schmitt, J. H. M. M. 2016, *A&A*, **585**, L2  
 Sanz-Forcada, J., Micela, G., Ribas, I., et al. 2011, *A&A*, **532**, A6  
 Schaefer, L., Wordsworth, R. D., Berta-Thompson, Z., & Sasselov, D. 2016, *ApJ*, **829**, 63  
 Shields, A. L., Ballard, S., & Johnson, J. A. 2016, *PhR*, **663**, 1  
 Sotin, C., Grasset, O., & Mocquet, A. 2007, *Icar*, **191**, 337  
 Tian, F., & Ida, S. 2015, *NatGe*, **8**, 177  
 Tilley, M. A., Segura, A., Meadows, V., Hawley, S., & Davenport, J. 2019, *AsBio*, **19**, 64  
 Torres, G., Kane, S. R., Rowe, J. F., et al. 2017, *AJ*, **154**, 264  
 Tuomi, M., Jones, H., Butler, R., et al. 2019, arXiv:1906.04644  
 Turbet, M., Bolmont, E., Ehrenreich, D., et al. 2020, *A&A*, **638**, A41  
 Vanderburg, A., Rowden, P., Bryson, S., et al. 2020, *ApJL*, **893**, L27  
 Watson, A. J., Donahue, T. M., & Walker, J. C. G. 1981, *Icar*, **48**, 150  
 West, A. A., Hawley, S. L., Bochanski, J. J., et al. 2008, *AJ*, **135**, 785  
 Wordsworth, R., & Pierrehumbert, R. 2013, *ApJ*, **778**, 154  
 Wordsworth, R., Schaefer, L., & Fischer, R. 2018, *AJ*, **155**, 195  
 Youngblood, A., France, K., Loyd, R. P., et al. 2017, *ApJ*, **843**, 31